Sensitivity-Bandwidth Limit in a Multimode Optoelectromechanical Transducer

I. Moaddel Haghighi,[1] N. Malossi,[1,2,†] R. Natali,[1,2] G. Di Giuseppe,[1,2] and D. Vitali[1,2,3,*]

[1]*School of Science and Technology, Physics Division, University of Camerino, I-62032 Camerino (MC), Italy*

[2]*INFN, Sezione di Perugia, I-06123 Perugia, Italy*

[3]*CNR-INO, Largo Enrico Fermi 6, I-50125 Firenze, Italy*

(Received 20 July 2017; revised manuscript received 6 November 2017; published 28 March 2018)

An optoelectromechanical system formed by a nanomembrane capacitively coupled to an LC resonator and to an optical interferometer has recently been employed for the highly sensitive optical readout of rf signals [T. Bagci *et al.*, Nature (London) **507**, 81 (2013)]. We propose and experimentally demonstrate how the bandwidth of such a transducer can be increased by controlling the interference between two electromechanical interaction pathways of a two-mode mechanical system. With a proof-of-principle device operating at room temperature, we achieve a sensitivity of 300 $\mathrm{nV}/\sqrt{\mathrm{Hz}}$ over a bandwidth of 15 kHz in the presence of radio-frequency noise, and an optimal shot-noise-limited sensitivity of 10 $\mathrm{nV}/\sqrt{\mathrm{Hz}}$ over a bandwidth of 5 kHz. We discuss strategies for improving the performance of the device, showing that, for the same given sensitivity, a mechanical multimode transducer can achieve a bandwidth significantly larger than that for a single-mode one.

DOI: 10.1103/PhysRevApplied.9.034031

I. INTRODUCTION

Optomechanical and electromechanical systems have recently experienced impressive development [1], and they have entered a quantum regime of late in which quantum states of nanogram-size mechanical resonators and/or electromagnetic fields have been generated and manipulated [2–10]. They have also been suggested for—and are already employed in—testing fundamental theories [11,12], and for quantum-limited sensing [13,14]. Furthermore, nanomechanical resonators can be simultaneously coupled to a large variety of different degrees of freedom, and they can therefore transduce signals at disparate frequencies with high efficiency [15–20], in either the classical or the quantum domain.

Reversible transduction between optical and radio-frequency–microwave (rf-MW) signals is currently particularly relevant, both in classical and quantum communication systems, and promising demonstrations with classical signals were recently conducted [21–23]. Specifically, the conversion of rf-MW signals into optical ones can be exploited for the highly sensitive detection of weak rf-MW signals by taking advantage of the fact that the homodyne detection of laser light can be quantum-noise limited with near-unit quantum efficiency. This transducer could help us to avoid many of the noise sources present for low-frequency signals and could be useful, for example, in radio astronomy, medical imaging, navigation, and classical and quantum communication.

Bagci *et al.* [21] reported a first important demonstration of this idea with an optical interferometric detection of rf signals with 800 $\mathrm{pV}/\sqrt{\mathrm{Hz}}$ sensitivity, which could be improved to 5 $\mathrm{pV}/\sqrt{\mathrm{Hz}}$ in the limit of strong electromechanical coupling. In this device, weak rf signals drive an LC resonator quasiresonantly interacting with a nanomechanical transducer, whose motion induces an optical phase shift which is then detected with quantum-limited sensitivity. An application of an optoelectromechanical transducer for nuclear-magnetic-resonance detection was recently demonstrated [24].

In Ref. [21], the detection bandwidth depends upon the LC bandwidth and the electromechanical coupling [17,21], and it is an important figure of merit in such transducers [25]. Finding systematic ways of increasing the detection bandwidth is of fundamental importance in many of the abovementioned applications: for example, more radio-astronomical sources could be detected, while, in communication networks, rf signals could be detected and processed more quickly.

Here, we show with a proof-of-principle experiment that a viable way to increase the bandwidth of optoelectromechanical transducers is to couple the LC circuit simultaneously to two (or more) mechanical modes with nearby frequencies, and to suitably engineer the two electromechanical couplings in order to realize constructive interference between the two rf-to-optical signal transductions mediated by each mechanical mode [see Fig. 1(a)].

*Corresponding author.
david.vitali@unicam.it
†Corresponding author.
nicola.malossi@unicam.it

Multimode optomechanical [26] and electromechanical [27–29] systems have recently been studied and utilized in a quantum regime, but here we exploit them with the aim of improving bandwidth and sensitivity of an optoelectromechanical transducer. The mechanical transducer is a (1×1)-mm SiN membrane of 50 nm thickness, coated with a 27-nm Nb film with a central circular hole (Norcada; see the inset of Fig. 1), capacitively coupled through Cu electrodes to an LC resonator and operated at room temperature. The mechanical modes exploited are the split doublet (1,2) and (2,1) revealed by optical homodyne detection. The achieved sensitivity of the two-mode transducer is 300 $\mathrm{nV}/\sqrt{\mathrm{Hz}}$ over a bandwidth of 15 kHz in the presence of rf noise, and the optimal shot-noise-limited sensitivity is 10 $\mathrm{nV}/\sqrt{\mathrm{Hz}}$ over a bandwidth of 5 kHz. The sensitivities are obtained in the case of electromechanical couplings for two modes equal to $G_1 = 118.41\ \mathrm{V\,m^{-1}}$ and $G_2 = -115.31\ \mathrm{V\,m^{-1}}$. However, as we show in Sec. II, the method is general and could be exploited to reach larger bandwidths at a sensitivity comparable to that of single-mode transducers [21].

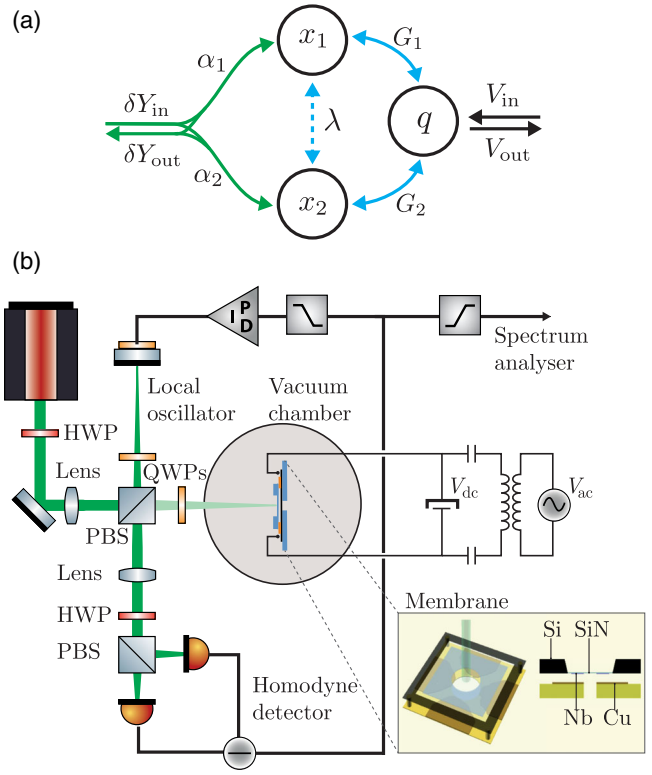

FIG. 1. (a) Scheme of the rf-to-optical transducer and of the interference between two transduction pathways through two mechanical modes, x_1 and x_2. The two modes are simultaneously capacitively coupled with the electromechanical couplings G_1 and G_2 to the same LC resonator q, and eventually through a direct mechanical interaction, λ. At the same time, the motion of the two resonators is read out by an optical interferometer using the light reflected from the membrane, δY_{out}, with optical couplings α_1 and α_2. Since modulation of the phase noise of the optical beam occurs through two different paths (via mode 1 or mode 2), the signal detected by the optical interferometer depends upon the interference between these two paths, which in turn can be controlled through the electrode configuration of the membrane capacitor. (b) Experimental setup. A rf resonator is constituted by an inductor and a membrane capacitor placed in a vacuum chamber evacuated at 1×10^{-7}. The mechanical displacement is revealed by homodyne detection of the light reflected by the membrane. The electromechanical coupling is controlled by applying a dc bias, V_{dc}, over two electrodes. The system is driven inductively through two capacitors, with a rf signal V_{ac} using an antenna. HWP, half wave plate; QWP, quarter wave plate; PBS, polarizing beam-splitter. (Inset) A (1×1)-mm SiN membrane coated with a 27-nm Nb film stands on top of four segment electrodes, forming a capacitor $C_m(x)$ modulated by the membrane motion.

This paper is organized as follows. In Sec. II, we introduce the multimode transducer theoretical framework. In Sec. III, we show and discuss the experimental result showing the performance of our device, and we also see how one can improve the design so that a two-mode transducer can achieve a larger bandwidth at the same sensitivity as a single-mode electromechanical transducer. Concluding remarks are provided in Sec. IV.

II. THEORETICAL FRAMEWORK

The system studied here is formed by a nanomechanical system capacitively coupled to an LC resonator. We generalize here the treatment of Ref. [21] to the multimode case. The nanomechanical system has a number of vibrational normal modes which can be described in terms of effective mechanical resonators with mass m_i, frequency ω_i, displacement x_i, and momentum p_i, so the effective Hamiltonian of the system is

$$H = \sum_i \frac{p_i^2}{2m_i} + \frac{m_i\omega_i^2 x_i^2}{2} + \frac{\phi^2}{2L} + \frac{q^2}{2C(\{x_i\})} - qV, \quad (1)$$

where ϕ is the flux in the inductor, q is the charge on the capacitors, and V is the voltage bias across the capacitor.

The coupling arises due to the displacement dependence of the capacitance $C(\{x_i\})$. This Hamiltonian directly leads to the Langevin equations

$$\dot{x}_i = \frac{p_i}{m_i}, \quad (2)$$

$$\dot{p}_i = -m_i\omega_i^2 x_i - \frac{q^2}{2}\frac{\partial}{\partial x_i}\left(\frac{1}{C(\{x_i\})}\right) - \Gamma_i p_i + F_i, \quad (3)$$

$$\dot{q} = \frac{\phi}{L}, \quad (4)$$

$$\dot{\phi} = -\frac{q}{C(x)} - \Gamma_{LC}\phi + V, \quad (5)$$

in which the terms corresponding to the damping rate Γ_i of the ith membrane mode and to the resistive dissipation rate $\Gamma_{LC} = R/L$ of the LC resonant circuit have been included, as well as driving forces F_i acting on each membrane mode.

Assuming that F_i represents zero-mean thermal Langevin forces, and writing the applied voltage as a large dc offset and a small fluctuating input

$$V(t) = V_{\rm dc} + \delta V(t), \tag{6}$$

we can linearize the Langevin equations around an equilibrium state of the system characterized by $(\bar{x}_i, \bar{p}_i, \bar{q}, \bar{\phi})$ and satisfying the conditions

$$\begin{aligned} m_i\omega_i^2\bar{x}_i &= -\frac{\bar{q}^2}{2}\frac{\partial}{\partial x_i}\left(\frac{1}{C(\{x_i\})}\right)\bigg|_{x_i=\bar{x}_i} \\ &= \frac{\bar{q}^2}{2}\frac{\partial C(\{x_i\})}{\partial x_i}\bigg|_{x_i=\bar{x}_i}\frac{1}{C(\{\bar{x}_i\})^2}, \end{aligned} \tag{7}$$

$$\bar{q} = V_{\rm dc}C(\{\bar{x}_i\}), \tag{8}$$

$$\bar{p}_i = \bar{\phi} = 0. \tag{9}$$

The dynamical equations for the small fluctuations, provided that the system is stable, are given by

$$\delta\dot{x}_i(t) = \frac{\delta p_i(t)}{m_i}, \tag{10}$$

$$\begin{aligned} \delta\dot{p}_i(t) = &-m_i\omega_i^2\delta x_i(t) \\ &\underbrace{-\frac{\bar{q}^2}{2}\frac{\partial^2}{\partial^2 x_i}\left(\frac{1}{C(\{x_i\})}\right)\bigg|_{x_i=\bar{x}_i}}_{2m\omega_i\Delta\omega_i}\delta x_i(t) \\ &\underbrace{-\frac{\bar{q}^2}{2}\sum\nolimits_{j\neq i}\frac{\partial^2}{\partial x_i\partial x_j}\left(\frac{1}{C(\{x_i\})}\right)\bigg|_{x_i=\bar{x}_i}}_{\lambda_{ij}}\delta x_j(t) \\ &-\Gamma_i\delta p_i - \underbrace{\bar{q}\frac{\partial}{\partial x_i}\left(\frac{1}{C(\{x_i\})}\right)\bigg|_{x_i=\bar{x}_i}}_{G_i}\delta q(t) + F_i, \end{aligned} \tag{11}$$

$$\delta\dot{q}(t) = \frac{\delta\phi(t)}{L}, \tag{12}$$

$$\begin{aligned} \delta\dot{\phi}(t) = &-\frac{\delta q(t)}{C(\{\bar{x}_i\})} - \Gamma_{LC}\delta\phi(t) + \delta V(t) \\ &-\sum_j \underbrace{\bar{q}\frac{\partial}{\partial x_j}\left(\frac{1}{C(\{x_i\})}\right)\bigg|_{x_i=\bar{x}_i}}_{G_j}\delta x_j(t). \end{aligned} \tag{13}$$

Here, we introduce the electromechanical coupling parameters

$$G_i = \bar{q}\frac{\partial}{\partial x_j}\left(\frac{1}{C(\{x_i\})}\right)\bigg|_{x_i=\bar{x}_i}, \tag{14}$$

the mechanical coupling between the vibrational normal modes induced by the second-order dependence of the capacitance upon the membrane deformation,

$$\lambda_{ij} = \frac{\bar{q}^2}{2}\sum_{j\neq i}\frac{\partial^2}{\partial x_i\partial x_j}\left(\frac{1}{C(\{x_i\})}\right)\bigg|_{x_i=\bar{x}_i}, \tag{15}$$

and the mechanical frequency shifts,

$$\Delta\omega_i = \frac{\bar{q}^2}{4m_i\omega_i}\frac{\partial^2}{\partial x_i^2}\left(\frac{1}{C(\{x_i\})}\right)\bigg|_{x_i=\bar{x}_i}. \tag{16}$$

Absorbing the frequency shifts into a redefined ω_i quantity and transforming to the Fourier domain yields

$$-i\Omega\delta x_i(\Omega) = \delta p_i(\Omega)/m_i, \tag{17}$$

$$\begin{aligned} -i\Omega\delta p_i(\Omega) = &-m_i\omega_i^2\delta x_i(\Omega) - \sum_j\lambda_{ij}\delta x_j(\Omega) \\ &-\Gamma_i\delta p_i(\Omega) - G_i\delta q(\Omega) + F_i(\Omega), \end{aligned} \tag{18}$$

$$-i\Omega\delta q(\Omega) = \delta\phi(\Omega)/L, \tag{19}$$

$$\begin{aligned} -i\Omega\delta\phi(\Omega) = &-\delta q(\Omega)/C - \Gamma_{LC}\delta\phi(\Omega) + \delta V(\Omega) \\ &-\sum_j G_j\delta x_j(\Omega). \end{aligned} \tag{20}$$

These algebraic equations can be used to calculate the response of the system to excitations through a force or voltage drive. For notational convenience, we define the susceptibilities

$$\chi_i(\Omega) = \frac{1}{m_i(\omega_i^2 - \Omega^2 - i\Omega\Gamma_i)}, \tag{21}$$

$$\chi_{LC}(\Omega) = \frac{1}{L(\Omega_{LC}^2 - \Omega^2 - i\Omega\Gamma_{LC})} \tag{22}$$

of the ith mechanical mode and of the LC resonator, respectively, and we define the circuit resonance frequency $\Omega_{LC} = (LC)^{-1/2}$. In the general case of many membrane modes, the solution can be easily derived when $\lambda_{ij} = 0$, i.e., without the direct mechanical coupling mediated by the capacitance and in the presence of only the indirect coupling through the LC resonator.

A. Two mechanical modes

We restrict ourselves now to the case of our system in which the detection bandwidth includes only two mechanical modes and where the effect of the other spectator modes

is negligible (i.e., it falls below the noise level). Using Eqs. (17)–(22), one can write

$$\chi_1(\Omega)^{-1}\delta x_1(\Omega) = -\lambda\delta x_2(\Omega) - G_1\delta q(\Omega) + F_1(\Omega), \quad (23)$$

$$\chi_2(\Omega)^{-1}\delta x_2(\Omega) = -\lambda\delta x_1(\Omega) - G_2\delta q(\Omega) + F_2(\Omega), \quad (24)$$

$$\chi_{LC}(\Omega)^{-1}\delta q(\Omega) = -G_1\delta x_1(\Omega) - G_2\delta x_2(\Omega) + \delta V(\Omega). \quad (25)$$

From the last equation, we have

$$\delta q(\Omega) = -\chi_{LC}(\Omega)[G_1\delta x_1(\Omega) + G_2\delta x_2(\Omega) - \delta V(\Omega)]. \quad (26)$$

Substituting in the first two, we get

$$\xi_1\delta x_1(\Omega) = \beta\delta x_2(\Omega) - G_1\chi_{LC}\delta V(\Omega) + F_1(\Omega), \quad (27)$$

$$\xi_2\delta x_2(\Omega) = \beta\delta x_1(\Omega) - G_2\chi_{LC}\delta V(\Omega) + F_2(\Omega), \quad (28)$$

with $\xi_i = \chi_i(\Omega)^{-1} - G_i^2\chi_{LC}(\Omega)$ and $\beta = [G_1G_2\chi_{LC}(\Omega) - \lambda]$. Then we have ($i = 1, 2$)

$$\delta x_i(\Omega) = \frac{\xi_{3-i}F_i(\Omega)}{\xi_1\xi_2 - \beta^2} + \frac{\beta F_{3-i}(\Omega)}{\xi_1\xi_2 - \beta^2} - \frac{\xi_{3-1}G_i + \beta G_{3-i}}{\xi_1\xi_2 - \beta^2}\chi_{LC}(\Omega)\delta V(\Omega). \quad (29)$$

The signal detected by the optical interferometer is the phase quadrature δY_{out} of the light reflected from the membrane, which can be written in the frequency domain as

$$\delta Y_{\text{out}}(\Omega) = \alpha_1\delta x_1(\Omega) + \alpha_2\delta x_2(\Omega) + \delta Y_{\text{in}}(\Omega); \quad (30)$$

that is, it is the sum of the vacuum phase noise, $\delta Y_{\text{in}}(\Omega)$, and the displacement fluctuations of the two mechanical modes weighted by the optomechanical couplings α_i, which depend upon the overlap of the selected membrane mode with the transverse profile of the optical field.

We calibrate the output signal as a displacement spectrum so that $\delta Y(\Omega)$ has the same units of $\delta x_j(\omega)$, that is, $\text{m}/\sqrt{\text{Hz}}$. As a consequence, the couplings α_j coincide with the dimensionless transverse overlap parameters defined in Eq. (A6) (see Appendix A). Using the fact that the four noises F_1, F_2, δV, and δY_{in} are uncorrelated, we can write the output optical phase spectrum as the sum of four independent terms,

$$S_{\text{out}}(\Omega) = \left|\frac{\alpha_1\xi_2 + \alpha_2\beta}{\xi_1\xi_2 - \beta^2}\right|^2 S_{F1}(\Omega) + \left|\frac{\alpha_2\xi_1 + \alpha_1\beta}{\xi_1\xi_2 - \beta^2}\right|^2 S_{F2}(\Omega) + S_{\text{in}}(\Omega) + \left|\frac{\alpha_1(\xi_2G_1 + \beta G_2) + \alpha_2(\xi_1G_2 + \beta G_1)}{\xi_1\xi_2 - \beta^2}\right|^2 \times |\chi_{LC}(\Omega)|^2 S_{\delta V}(\Omega), \quad (31)$$

where $S_{Fj}(\Omega) = 2m_j\Gamma_j k_B T$ and $j = 1, 2$ are the Brownian-force noise spectra, T is the system temperature, $S_{\delta V}(\Omega)$ is the noise voltage at the input of the LC circuit, and $S_{\text{in}}(\Omega)$ is the optical shot-noise spectrum.

Let us now try to readjust and rewrite this general expression for the detected spectrum in order to get some physical intuition from it. We first define the effective mechanical susceptibilities of the two modes, modified by the interaction with the LC circuit ($i = 1, 2$),

$$\chi_i^{\text{eff}}(\Omega) = \frac{\xi_{3-i}}{\xi_1\xi_2 - \beta^2}, \quad (32)$$

$$[\chi_i^{\text{eff}}(\Omega)]^{-1} = \chi_i^{-1}(\Omega) - G_i^2\chi_{LC}(\Omega) - \frac{\beta^2}{\chi_{3-i}^{-1}(\Omega) - G_{3-i}^2\chi_{LC}(\Omega)}. \quad (33)$$

The detected spectrum of Eq. (31) can then be rewritten as

$$S_{\text{out}}(\Omega) = |\alpha_1 + \alpha_2\mu_2(\Omega)|^2|\chi_1^{\text{eff}}(\Omega)|^2 S_{F1}(\Omega) + |\alpha_2 + \alpha_1\mu_1(\Omega)|^2|\chi_2^{\text{eff}}(\Omega)|^2 S_{F2}(\Omega) + |I(\Omega)|^2|\chi_{LC}(\Omega)|^2 S_{\delta V}(\Omega) + S_{\text{in}}(\Omega), \quad (34)$$

where

$$I(\Omega) = \alpha_1\chi_1^{\text{eff}}(\Omega)[G_1 + G_2\mu_2(\Omega)] + \alpha_2\chi_2^{\text{eff}}(\Omega)[G_2 + G_1\mu_1(\Omega)], \quad (35)$$

with

$$\mu_i(\Omega) = \frac{\beta}{\xi_i} = \frac{G_1G_2\chi_{LC}(\Omega) - \lambda}{\chi_i(\Omega)^{-1} - G_i^2\chi_{LC}(\Omega)}. \quad (36)$$

It is evident from Eq. (34) that the transduction of voltage input signals into the optical output signal is determined mainly by the quantity $I(\Omega)$ of Eq. (35), which is the sum of the two mechanical resonator contributions, i.e., the result of the interference between the two excitation pathways associated with each mechanical mode of Fig. 1(a). The quantity $|I(\Omega)|$ determines the voltage sensitivity of the transducer, and a larger $|I(\Omega)|$ value indicates a higher sensitivity for our transducer; therefore, one has to engineer the couplings G_j in order to realize constructive interference between the transduction of the two modes and maximize $|I(\Omega)|$.

The explicit expression of the detected spectrum at the output of the transducer simplifies considerably in the following limit: (i) $\lambda = 0$ (which we verify is actually satisfied by our experimental setup with a very good approximation), and (ii) we stop at first order in G_i; i.e., we neglect second-order terms in G_i. In this limit, $\chi_i^{\text{eff}}(\Omega) \to \chi_i(\Omega)$ and $\mu_i(\Omega) = 0$, and one has the following

much-simpler output spectrum, and a simpler form of the interference function $I(\Omega)$ in particular:

$$S_{\rm out}(\Omega) = |\alpha_1|^2|\chi_1(\Omega)|^2 S_{F1}(\Omega) + |\alpha_2|^2|\chi_2(\Omega)|^2 S_{F2}(\Omega) + S_{\rm in}(\Omega) + |\alpha_1 G_1\chi_1(\Omega) + \alpha_2 G_2\chi_2(\Omega)|^2|\chi_{LC}(\Omega)|^2 S_{\delta V}(\Omega). \quad (37)$$

The amplitudes and the relative signs of the couplings G_1, α_1, G_2, and α_2 determine the output spectrum—and therefore the behavior of the transducer itself. In fact, since the two effective mechanical susceptibilities $\chi_j(\Omega)$ halfway between the two mechanical resonance peaks are real and have the opposite signs, we see from Eq. (37) that the products $\alpha_1 G_1$ and $\alpha_2 G_2$ must have the same sign, in the case of destructive interference, and opposite signs, in the case of constructive interference, between the two transduction pathways. In the first case, we would observe a spectrum region where the rf signal is canceled out by the destructive interference between the transduction of the two mechanical modes. In the second case, we would observe a spectrum region between the two resonance peaks where the output signal is flat and is enhanced by the constructive interference between the two electromechanical couplings. Experimentally, we observe both behaviors. We refer the reader to Sec. III for further details and discussion.

B. Relation between sensitivity and bandwidth

The transducer voltage sensitivity can be quantified by appropriately rescaling the detected noise spectrum of Eqs. (34) and (37), i.e., by defining the spectral voltage sensitivity as [21]

$$\sqrt{S_{\delta V}^{\rm out}(\Omega)} = \frac{\sqrt{S_{\rm out}(\Omega)}}{|I(\Omega)||\chi_{LC}(\Omega)|}. \quad (38)$$

One expects that the better the sensitivity, the narrower the corresponding bandwidth; we confirm that this is, in fact, the case by quantifying this trade-off with a simple formula that is valid for the constructive interference case.

Equation (38) shows us that the minimum detectable voltage signal corresponds to the situation of minimum output noise $S_{\rm out}(\Omega)$, and the maximum value of the product $|I(\Omega)||\chi_{LC}(\Omega)|$. Minimum output noise is achieved when the contribution of all technical noises, that is, thermal and rf ones, are negligible with respect to the unavoidable shot-noise contribution, i.e., when the first, second, and fourth terms in Eq. (37) are negligible with respect to the third term, so that $S_{\rm out}(\Omega) \simeq S_{\rm in}(\Omega)$. The denominator of Eq. (38) is instead maximal when the LC circuit resonance peak (which is typically much broader than the mechanical peaks) is centered between the mechanical doublet, and when $|I(\Omega)|$ is largest, showing why constructive interference is needed for a sensitive transducer.

Actually, $|I(\Omega)|$ is exactly maximal at the two mechanical resonance frequencies, where, in principle, one can get the best sensitivity. However, in order to get a physically meaningful and practical estimation of the optimal detectable voltage, we make here a conservative choice and consider the flat response region obtained by constructive interference between the two mechanical resonances.

In fact, the latter resonances do not represent a convenient working point because they are very narrow and are extremely sensitive to small frequency shifts, and one expects a quite unstable transducer response there (see also the experimental results in Sec. III). Therefore, we take as the optimal detectable signal the expression of Eq. (38) when $S_{\rm out}(\Omega) \simeq S_{\rm in}(\Omega)$, evaluated halfway between the two mechanical resonances, at $\bar{\Omega} = (\omega_1 + \omega_2)/2$,

$$\sqrt{S_{\delta V}^{\rm opt}(\bar{\Omega})} = \frac{\sqrt{S_{\rm in}(\bar{\Omega})}}{|I(\bar{\Omega})|\chi_{LC}(\bar{\Omega})|}. \quad (39)$$

In the simple case of a symmetric electromechanical system, that is, by assuming same masses ($m = m_1 = m_2$), electromechanical couplings ($G = |G_1| = |G_2|$), and damping rates ($\Gamma = \Gamma_1 = \Gamma_2$) for the two mechanical modes, and assuming also optimal optical detection ($\alpha = \alpha_1 = \alpha_2 = 1$), $I(\bar{\Omega})$ is given by

$$|I(\bar{\Omega})| = \frac{G}{m\bar{\Omega}}\left|\frac{1}{i\Gamma + \Delta\Omega} - \frac{1}{i\Gamma - \Delta\Omega}\right|, \quad (40)$$

where $\Delta\Omega = \omega_2 - \omega_1$. In typical situations, one has $\Delta\Omega \gg \Gamma$, so one can safely write

$$|I(\bar{\Omega})| = \left(\frac{2G}{m\bar{\Omega}\Delta\Omega}\right), \quad (41)$$

and, substituting the latter expression into Eq. (39), one finally gets the desired sensitivity-bandwidth-ratio limit

$$\frac{\sqrt{S_{\delta V}^{\rm opt}}}{\Delta\Omega} = \frac{m\bar{\Omega}\sqrt{S_{\rm in}(\bar{\Omega})}}{2|G\chi_{LC}(\bar{\Omega})|}. \quad (42)$$

This relation shows that, as expected, there is a trade-off between the voltage sensitivity and the bandwidth for an optoelectromechanical transducer with a given set of parameters. We can also see that, for a given shot-noise level and fixing a desired voltage sensitivity $S_{\delta V}^{\rm opt}$, one can increase the bandwidth either by decreasing the mechanical resonator mass or by increasing the electromechanical coupling, always keeping the LC circuit at resonance so that $|\chi_{LC}|$ is maximal.

III. EXPERIMENT

A schematic description of the experiment is given in Fig. 1(b). A laser at 532 nm is split into a 10-mW beam (a local oscillator), and a few-hundred-microwatt one for probing the mechanical oscillator. The beam reflected by the membrane is superposed to the local oscillator for detecting the phase fluctuations. The low-frequency region of the voltage spectral noise of the homodyne signal is exploited to lock the interferometer to the gray fringe (i.e., in the condition where the interferometer output is proportional to the membrane displacement) by means of a proportional-integral-derivative controller. The thermal displacement of the metalized membrane modes are revealed in the high-frequency range, as shown in Fig. 2 (bottom panel).

Calibration and fitting of the enlarged spectra of the fundamental and doublet modes shown in Fig. 2 (top panels) allows us to obtain the optical masses $m_{\rm opt}^{(1,1)}$, $m_{\rm opt}^{(1,2)}$, and $m_{\rm opt}^{(2,1)}$ of each mode. As explained in Appendix A, they are given by $m_{\rm opt}^{(i,j)} = m_{\rm eff}/\alpha_{(\rm i,j)^2}$, that is, by the effective mass of these three membrane modes, which are all equal, divided by the square of the respective optomechanical coupling. One can estimate from them the most likely value of the center of the laser beam (and therefore of the optomechanical couplings $\alpha_{(\rm i,j)}$), and of the effective mass. The latter is equal to $m_{\rm eff} \simeq 67.3$ ng, in very good agreement with the prediction made from a finite-element method (FEM) numerical analysis of the metalized membrane (see Fig. 2, middle panel).

The membrane is placed on top of a four-segment copper electrode to form a variable capacitor $C_m(\{x_i\})$, which depends upon the transversal displacement of the membrane, and therefore on the two mode displacements, x_i. The distance h_0 between the metalized membrane and the four-segment electrodes is determined to be $31.0(1)$ μm by the measurement of the frequency shift of the membrane fundamental mode (1,1) as a function of the applied $V_{\rm dc}$, and the estimation of the effective area of the membrane capacitor (see Appendix B and Ref. [21]). This capacitor is added in parallel to the rest of capacitors of the LC circuit C_0, and the total capacitance, $C(\{x_i\}) = C_0 + C_m(\{x_i\})$, is connected in parallel to a ferrite-core inductor with an inductance of $L \simeq 427$ μH. Taking into account the total series resistance of contacts and wires R, we have an LC resonator with the resonance frequency $\Omega_{LC}/2\pi \simeq 383$ kHz, which is therefore quasiresonant with the two mechanical modes, and a quality factor $Q \simeq 81$.

We study the behavior of our device as a high-sensitive optical detector of rf signals by fixing the applied dc bias at $V_{\rm dc} = 270$ V. A broadband rf signal is injected into the system inductively using an auxiliary inductor in front of the main LC inductor, and the corresponding displacement spectral noise (DSN) is detected. The nonzero voltage bias couples the LC circuit with the two mechanical modes whose motion, in turn, modulates the phase of the light; as a result, the input rf signal is transduced as an optical phase modulation readout by the interferometer. The results are shown in Fig. 3, where the two plots correspond to two different electrode configurations.

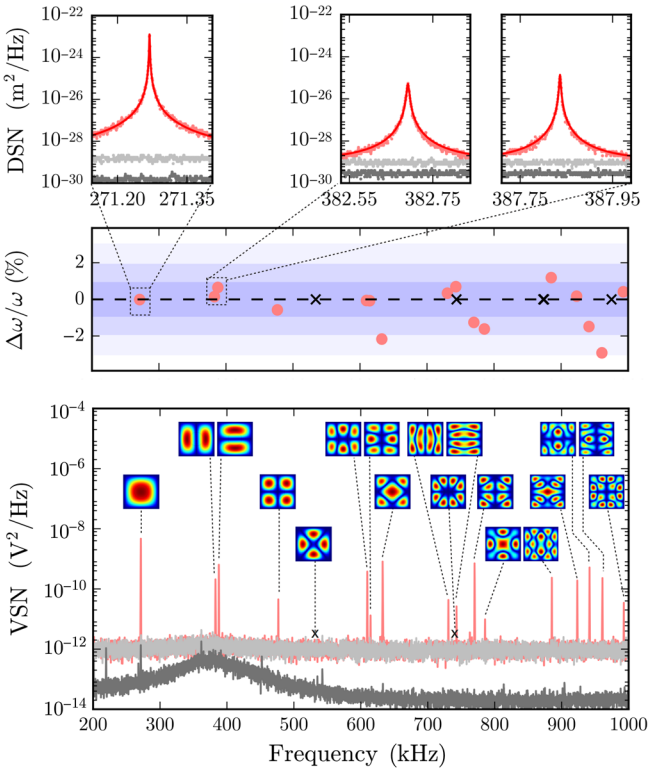

FIG. 2. (Top panels) Calibrated displacement spectral noise (DSN) obtained from the homodyne measurement of the optical output when the system is driven by thermal noise only, i.e., without any electromechanical coupling. (Top-left panel) DSN of the first mode (the light-red dots) and the theoretical curve (the red line) obtained with the best-fit values $\omega_m^{(1,1)} = 2\pi \times 271.269$ kHz, $\Gamma^{(1,1)} = 2\pi \times 0.9$ Hz, and $m_{\rm opt}{}^{(1,1)} = 70.0(2)$ ng. (Top-right panel) The mode doublet exploited for the transduction, with best-fit values $\omega_m^{(1,2)} = 2\pi \times 382.690$ kHz, $\Gamma^{(1,2)} = 2\pi \times 4.9$ Hz, $m_{\rm opt}^{(1,2)} = 1.73(1)$ μg, and $\omega_m^{(2,1)} = 2\pi \times 387.836$ kHz, $\Gamma^{(2,1)} = 2\pi \times 2.6$ Hz, $m_{\rm opt}^{(2,1)} = 1.18(1)$ μg (see Appendix A). (Middle panel) Relative error between the detected frequencies (obtained from the peaks within the broader homodyne spectrum shown at the bottom of the figure) and those obtained from a numerical finite-element analysis of the vibrational modes of the metalized membrane. The relative error found for the first five detected modes is less than 1%, and for the higher modes less than 3%. The black crosses indicate modes which are uncoupled to the light beam and are therefore unobservable. (Bottom panel) Voltage spectral noise (VSN) of the homodyne signal. Each peak is associated with the corresponding vibrational mode shape obtained from the finite-element analysis. Light-gray and dark-gray curves denote shot- and electronic-noise contributions, respectively.

The comparison evidences that by changing the electrodes on which the bias voltage is applied, we are able to control the interference between the two

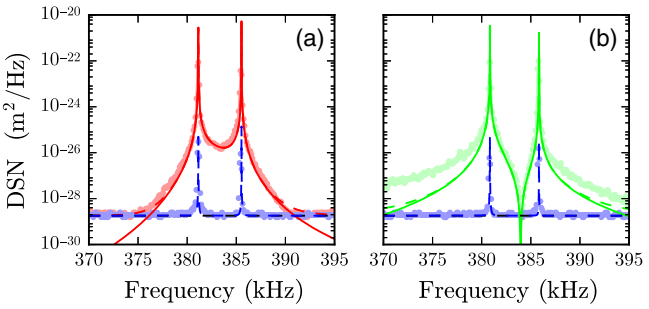

FIG. 3. Displacement spectral noise (DSN). Light-red and light-green dots correspond to the detection of (a) constructive and (b) destructive interference between the two mechanical transduction pathways, respectively, in the presence of an applied voltage bias $V_{dc} = 270$ V and an input rf signal. The light-blue dots refer to the optical output spectrum due to thermal noise and without any rf input to the LC circuit. The solid red and green lines are the theoretical expectations without noise. The dashed red, green, and blue lines account for the shot-noise contribution.

transduction pathways associated with each mechanical mode schematically illustrated in Fig. 1. Specifically, by changing the electrodes, we are able to change the effective areas of the membrane capacitor, thereby changing the relative sign between the two electromechanical couplings G_1 and G_2 (see Appendix B). As discussed in Sec. II, this relative sign flip corresponds to switching from constructive interference [Fig. 3(a)] to destructive interference [Fig. 3(b)]. In fact, in our case, the two optomechanical couplings α_i are positive numbers (see below), and G_1 and G_2 have the same sign in the case of destructive interference [Fig. 3(b)], and opposite signs in the case of constructive interference [Fig. 3(a)]. This fact is confirmed by the theoretical curves which best overlap with the experimental data, corresponding to the following values of the electromechanical couplings: $G_1 = 118.41\ \mathrm{V\,m^{-1}}$ and $G_2 = -115.31\ \mathrm{V\,m^{-1}}$ for the red line in Fig. 3(a), and $G_1 = 117.63\ \mathrm{V\,m^{-1}}$ and $G_2 = 110.89\ \mathrm{V\,m^{-1}}$ for the green line in Fig. 3(b). These values are confirmed within an 8% error, with an independent method based on the explicit evaluation of the membrane-electrode capacitance and its derivatives from the knowledge of the device geometry (see Appendix B and Ref. [21]). This geometrical estimation of the electromechanical coupling crucially depends upon the overlap between the electrodes and the positive and negative portions of the chosen membrane vibrational eigenmode, and it therefore also provides an idea of how one can control the relative sign between the two electromechanical couplings by applying the voltage bias to different electrodes.

The position of the laser beam with respect to the membrane determines the transverse overlap between the optical laser field and each mechanical mode—and therefore the optomechanical couplings α_i giving the weight of the two interference pathways. As shown in Appendix A, we find for the constructive interference case the best values $\alpha_1 = 0.196$ and $\alpha_2 = 0.240$, while, for destructive interference, we find $\alpha_1 = 0.196$ and $\alpha_2 = 0.121$. The theoretical prediction is less accurate away from the mechanical resonances for the destructive case; in the latter case, in fact, one has constructive interference effects between the doublet modes and the fundamental and higher mechanical modes, which are not fully taken into account by our model.

We remark that the possibility of tuning the performance of our two-mode transducer by controlling the relative sign of the electromechanical couplings and the associated interference effect is available only when the two mechanical modes are simultaneously coupled to *two distinct* electromagnetic modes. In fact, if we were to simplify the scheme and use a *unique* electromagnetic (either radio-frequency or optical) mode both for coupling the modes and reading out the signals, we would always get a destructive interference pattern in the output spectrum, and the constructive case of Fig. 3(a) would be impossible. In such a case, α_i and G_i ($i = 1, 2$) share the same sign, and therefore the response of the two mechanical modes in the frequency band within the two resonances is always out of phase [30,31]. Our two-mode transducer is analogous to the devices recently proposed in Refs. [32–34] for nonreciprocal conversion between microwave and optical photons, and demonstrated in Refs. [33,35], in which two mechanical modes are simultaneously coupled via four appropriate drives with two different microwave cavity modes, for nonreciprocal signal conversion between the latter. In our case, the configuration corresponding to the constructive interference of Fig. 3(a) realizes the unidirectional transduction of rf signals into optical ones, while the one corresponding to the destructive interference of Fig. 3(b) realizes an isolator which, within the bandwidth where $I(\Omega) \simeq 0$, inhibits the transmission of rf signals to the optical output. The device demonstrated here has the advantage that it does not require driving with four different tones and the validity of the rotating-wave approximation. Moreover, the device is easily reconfigurable because one can switch from one configuration to the other by simply switching electrodes [36].

As we discuss in Sec. II, under the condition of constructive interference, the mechanical modes are responsible for an improved transduction of rf signals into the optical output within the frequency band between the two mechanical resonances. Therefore, we expect that, under the conditions of Fig. 3(a), the device acts as a transducer with an increased bandwidth. This improvement is confirmed by Fig. 4, where we show the voltage sensitivity (VS) defined in Eq. (38), i.e., the minimum detectable voltage, corresponding to the total noise spectrum of Fig. 3(a) divided by the interface response function. The light-red circles correspond to the broader band voltage sensitivity of our transducer, which is equal to

300 nV/$\sqrt{\text{Hz}}$ over a bandwidth of 15 kHz between the two modes, obtained in the case where rf noise dominates over thermal and shot noise. The blue dots and lines instead correspond to the optimal sensitivity of our device, which is around 10 nV/$\sqrt{\text{Hz}}$ over a bandwidth of 5 kHz, achieved in the opposite limit when the contribution of the input rf noise is negligible with respect to the thermal and shot noise. In the latter limit, in the flat region between the two resonance peaks, thermal noise is also negligible, and the data (the blue dots) exactly satisfy the optimal sensitivity-bandwidth ratio of Eq. (42). Conversely, the data (the red dots) in the presence of a non-negligible noise contribution from the *LC* circuit corresponds to a larger value for the sensitivity-bandwidth ratio compared to the optimal value. For example, in Fig. 4, the red data correspond to a bandwidth ratio 10 times larger than the optimal one achieved for the blue data.

For comparison, in Fig. 5 we show the minimum detectable voltage in the *destructive* interference case of Fig. 3(b). Even though, in the case of large rf noise, we have a sensitivity of about 300 nV/$\sqrt{\text{Hz}}$, which is comparable to that of the constructive interference case, the situation is completely different in the regime of negligible rf input noise (the blue dots and the theoretical curve). As expected, in the latter case, the sensitivity significantly worsens between the two mechanical resonances, and the minimum detectable voltage tends to diverge in correspondence to the destructive interference condition, where the device acts as an isolator with respect to the rf input. It is evident that, in the presence of destructive interference, the device cannot be operated as a rf-to-optical transducer, and that a sensitivity-bandwidth ratio cannot even be defined here.

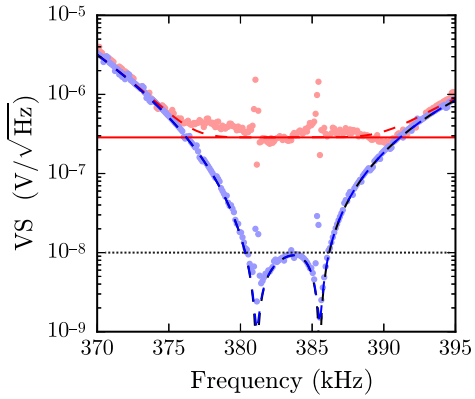

FIG. 4. Voltage sensitivity (VS) of the rf-to-optical transducer. The light-red dots correspond to the inferred voltage sensitivity of our transducer from the blue data of Fig. 3(a), that is, the square root of the DSN divided by the interface response function, which is equal to 300 nV/$\sqrt{\text{Hz}}$ over a bandwidth of 15 kHz. The light-blue dots represent the optimal sensitivity achieved by our device in the case of negligible rf noise, equal to 10 nV/$\sqrt{\text{Hz}}$ over a bandwidth of 5 kHz (the dotted black line). The dashed and solid lines represent the corresponding theoretical expectations, as in Fig. 3. In the latter case, the sensitivity-bandwidth ratio is in agreement with the optimal limit given by Eq. (42).

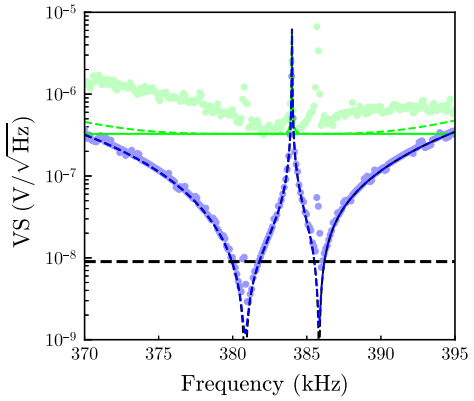

FIG. 5. Voltage sensitivity (VS) of the rf-to-optical transducer in the presence of destructive interference, from the data of Fig. 3(b). The light-green dots correspond to the inferred voltage sensitivity of our transducer, that is, the square root of the DSN divided by the interface response function, which is equal to 300 nV/$\sqrt{\text{Hz}}$ over a bandwidth approximately equal to 5 kHz. The light-blue dots represent the sensitivity achieved in the case of negligible rf noise, which tends to diverge at the frequencies where one has destructive interference and the device is not sensitive to the input rf signal. The dashed and solid lines represent the corresponding theoretical expectations.

We also remark that the present transducer can also be treated as a radio-frequency amplifier, transforming a voltage input signal into a voltage signal at the output of the optical detector, but at a much higher signal-to-noise ratio, with a given gain and a given input impedance. At the working point described here and corresponding to Figs. 4 and 5, we measure for our device a gain of 30 dB at the mechanical frequencies, and a gain of 10 dB in the frequency range between them. Moreover, we characterize the input impedance by obtaining a value $Z_{\text{in}} = (51.2 + 19.5i)$ kΩ.

A. Improving the two-mode transducer performance

Using the theoretical description provided in Sec. II, we now see how much one could improve the performance of our transducer in the constructive interference configuration. The voltage sensitivities achievable in a device similar to that experimentally demonstrated here, but with tunable electromechanical couplings $|G_1| = |G_2| = G$ and frequency separation $\Delta\nu_m = [\omega_m^{(2,1)} - \omega_m^{(1,2)}]/2\pi$, are shown in Fig. 6. We show the transducer voltage sensitivity as a function of the electromagnetic coupling G at a fixed mechanical-mode frequency separation $\Delta\nu_m$ in Fig. 6(a), and versus the mechanical-mode splitting at a fixed G in Fig. 6(b) in the case of negligible rf noise.

The voltage sensitivity is calculated from Eqs. (34) and (38) while considering the following experimental parameters: equal effective mass $m_{\text{eff}} = 67.3$ ng, equal

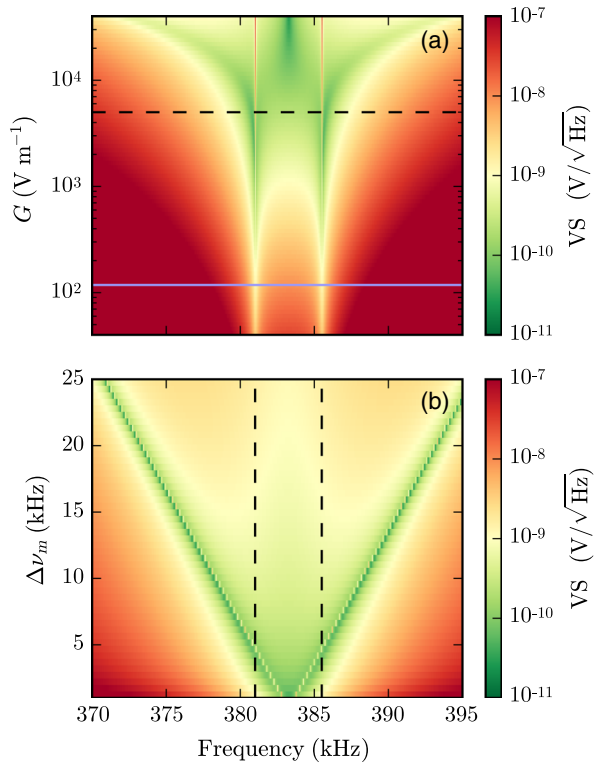

FIG. 6. Theoretical prediction for the voltage sensitivity (VS) of a rf-to-optical transducer based on a two-mode mechanical resonator in the case of negligible rf noise with a shot-noise level $S_{\text{in}} = 1.8 \times 10^{-29}$ m^2/Hz. (Top panel) VS as a function of the frequency and of the electromechanical coupling G (assumed to be equal in modulus for the two modes). The other parameters are chosen to be very close to those of our experimental device. The two vertically brighter features represent the mechanical-mode resonance frequencies at $\omega_m^{(1,2)} = 2\pi \times 381$ kHz and $\omega_m^{(2,1)} = 2\pi \times 385.5$ kHz, with the same damping rate $\Gamma_m^{(1,2)} = \Gamma_m^{(2,1)} = 2\pi \times 3.6$ Hz, the same effective mass $m_{\text{eff}} = 67.3$ ng, and the same optomechanical coupling $\alpha_1 = \alpha_2 = 0.194$. The LC circuit resonates at $\omega_{LC} = (\omega_m^{(1,2)} + \omega_m^{(2,1)})/2$ with a quality factor $Q = 81.5$. The blue solid line denotes the electromechanical coupling in our device, $G = 118$ V m^{-1}, while the black dashed line denotes the value $G = 5$ kV m^{-1} needed to obtain a mean voltage sensitivity on the order of 1 nV/$\sqrt{\text{Hz}}$ over a bandwidth of 15 kHz. For larger G values, both the sensitivity and the bandwidth increase. (Bottom panel) VS as a function of the frequency and of the mechanical-mode separation $\Delta\nu_m = (\omega_m^{(2,1)} - \omega_m^{(1,2)})/2\pi$ evaluated for the same parameters as the plot above, with a value of the electromechanical coupling G indicated by the black dashed line of the top figure. The vertical black dashed lines represent the two resonance frequencies chosen above. We see that one can achieve and maintain a voltage sensitivity of around 1 nV/$\sqrt{\text{Hz}}$ over a bandwidth which increases with increasing frequency separation between the two mechanical modes.

mechanical damping rates $\Gamma = 2\pi \times 3.6$ Hz, equal optomechanical couplings $\alpha_1 = \alpha_2 = 0.194$, an LC circuit resonating halfway between the two mechanical resonances with a quality factor $Q = 81.5$, and a shot-noise level $S_{\text{in}} = 1.8 \times 10^{-29}$ m^2/Hz. In Fig. 6(a), the two resonance frequencies are fixed at $\omega_m^{(1,2)}/2\pi = 381$ kHz and $\omega_m^{(2,1)}/2\pi = 385.5$ kHz. The solid blue line denotes the electromechanical coupling in our device, $G = 118$ V m^{-1}, while the dashed line denotes the electromechanical coupling $G = 5$ kV m^{-1}, which is used to calculate Fig. 6(b). Figure 6(a) shows that, as expected, both the sensitivity and the bandwidth can be increased by increasing the electromechanical coupling and that one can achieve sensitivities comparable to those of Ref. [21] over a larger bandwidth in the strong-coupling regime where the LC and the mechanical modes hybridize, which occurs in our case when $G > 10$ kV m^{-1}.

A feasible way to achieve these values for the coupling is to decrease the distance d between the electrodes and the metalized SiN membrane since the coupling scales as the inverse square of d, and this strong-coupling regime could be achieved with a distance $d \simeq 3$ μm. Figure 6(b) instead shows that, even in a regime away from the strong-coupling regime, the transduction bandwidth can be increased simply by increasing the mechanical-mode frequency splitting.

With a coupling $G = 5$ kV m^{-1}, about a factor of 30 larger than the one showed by our device, a sensitivity on the order of 1 nV/$\sqrt{\text{Hz}}$ is reachable over a bandwidth that depends essentially only upon the mechanical-mode splitting. In practice, by improving the device demonstrated here, for example, by operating at a membrane capacitor distance of around $d \simeq 3$ μm in order to reach $G \simeq 10$ kV m^{-1} and increasing the mechanical-mode frequency splitting by using a rectangular membrane of (0.9×1.1)-mm sides, one could achieve the same sensitivity of 800 pV/$\sqrt{\text{Hz}}$ as Ref. [21] over a larger bandwidth of 40 kHz.

IV. CONCLUSIONS

We theoretically show and experimentally demonstrate in this paper that one can engineer constructive interference between two or more mechanical modes coupled to the same resonant LC circuit in order to increase the transduction bandwidth of a rf-to-optical transducer with a target voltage sensitivity equal to that of a single-mechanical-mode transducer. We present here a proof-of-principle experiment with a first-generation device proving the reliability of the proposed technique and its physical insight. We see that an improved version of the same device could outperform an existing single-mode optoelectromechanical transducer in terms of sensitivity—and especially in terms of bandwidth.

The proposed multimode transducer based on constructive interference is advantageous and more flexible than the one based on a single mechanical mode. In fact, in single-mode optoelectromechanical transducers, bandwidth and sensitivity are strongly related and are determined only by electromechanical coupling. In the case of capacitive

coupling, it is extremely hard to achieve very large values for such a coupling because the bias voltage and the membrane capacitor area cannot be too large, and it is hard to reach membrane capacitor distances well below 1 μm.

On the contrary, in multimode optoelectromechanical transducers in the constructive interference configuration, for a given voltage sensitivity, the bandwidth is determined mainly by the mechanical frequency splitting, and it therefore can be significantly increased even without entering the strong electromechanical coupling regime.

ACKNOWLEDGMENTS

We acknowledge the support of the European Commission through the ITN–Marie Curie project "Cavity Quantum Optomechanics" (cQOM), FP7 FET-Open Project No. 323924 "Interfacing Quantum Optical, Electrical, and Mechanical Systems" (iQUOEMS), and H2020–FETPROACT–2016 Project No. 732894 "Hybrid Optomechanical Technologies" (HOT). We also thank Norcada for providing us the Nb metalized SiN membranes.

APPENDIX A: DATA ANALYSIS

1. Determination of mechanical parameters from thermal-noise spectra

The mechanical properties of the membrane vibrational modes, that is, their resonance frequency, damping rate, and mass, can be extracted from the measured homodyne spectra in the presence of thermal noise only—that is, in the absence of the electromechanical coupling—occurring when $V_{\rm dc}=0$ and the rf signal is turned off. For a generic harmonic oscillator of mass m, frequency ω_m, and damping Γ in the presence of thermal noise at temperature T, the variance of its mechanical displacement, $\langle x^2\rangle = k_B T/m\omega_m^2$, is related to the DSN $S_{xx}(\omega)$ by the relation

$$\langle x^2\rangle = \int_{-\infty}^{+\infty} S_{xx}(\omega)\frac{d\omega}{2\pi} = \int_0^{+\infty} \bar{S}_{xx}(\nu)d\nu, \quad \text{(A1)}$$

where

$$S_{xx}(\omega) = \frac{2m\Gamma k_B T}{|m(\omega_m^2-\omega^2-i\omega\Gamma)|^2}, \quad \text{(A2)}$$

and, defining $\omega = 2\pi\nu$, $\omega_m = 2\pi\nu_m$, and $\Gamma = 2\pi\gamma$, one has

$$\bar{S}_{xx}(\nu) = \frac{1}{\pi m}\frac{2\gamma k_B T}{|\nu_m^2-\nu^2-i\nu\gamma|^2}. \quad \text{(A3)}$$

The *measured* DSN, $\bar{S}_{xx}^{(m)}(\nu)$, is obtained from the calibration of the voltage spectral noise $S_{VV}(\nu)$ that is effectively detected at the output of our optical interferometer,

$$\bar{S}_{xx}^{(m)}(\nu) = S_{VV}(\nu)G_{xV}^2, \quad \text{(A4)}$$

with the calibration factor $G_{xV}=\lambda/(2\pi V_{\rm pp})$, where $\lambda = 532$ nm is the laser wavelength used and $V_{\rm pp}$ is the peak-to-peak voltage value of the interferometer interference fringes. Then the measured DSN is fitted with the theoretical $\bar{S}_{xx}(\nu)$ of Eq. (A3) obtaining the best-fit values for ω_m and Γ.

Because of the effect of the optical transduction [see Eq. (30)], for each mechanical mode, the fit provides for the mass the value of what can be called the *optical* mass $m_{\rm opt}^{(n,m)}$, which is related to the physical effective mass of each mode and the optomechanical coupling $\alpha_{(n,m)}$ by the relation $m_{\rm opt}^{(n,m)} = m_{\rm eff}^{(n,m)}/\alpha_{(n,m)}^2$. The variance of the mechanical displacement $\langle x^2\rangle$ is instead equal to the size of the step in the measured displacement noise (DN), that is, the marginal of the DSN (see the blue curves in Figs. 7 and 8). We perform such a fit for the fundamental vibrational mode of the membrane (1,1) (see Fig. 7), and for the first excited vibrational doublet (1,2) and (2,1) exploited here for our transducer (see Fig. 8).

For the (1,1) mode we obtained the best-fit values $\omega_m^{(1,1)} = 2\pi\times 271.269$ kHz, $\Gamma^{(1,1)} = 2\pi\times 0.9$ Hz, and $m_{\rm opt}^{(1,1)} = 70.0(2)$ ng. The size of the step in the DN yields $\langle x^2\rangle^{(1,1)} \simeq 24.18$ pm^2. For the (1,2)-(2,1) doublet, we instead obtain the best-fit values $\omega_m^{(1,2)} = 2\pi\times 382.690$ kHz, $\Gamma^{(1,2)} = 2\pi\times 4.9$ Hz, $m_{\rm opt}^{(1,2)} = 1.73(1)$ μg, and $\omega_m^{(2,1)} = 2\pi\times 387.836$ kHz, $\Gamma^{(2,1)} = 2\pi\times 2.6$ Hz, $m_{\rm opt}^{(2,1)} = 1.18(1)$ μg. The variances of the mechanical displacement are $\langle x^2\rangle^{(1,2)} \simeq 0.397$ pm^2, and $\langle x^2\rangle^{(2,1)} \simeq 0.590$ pm^2.

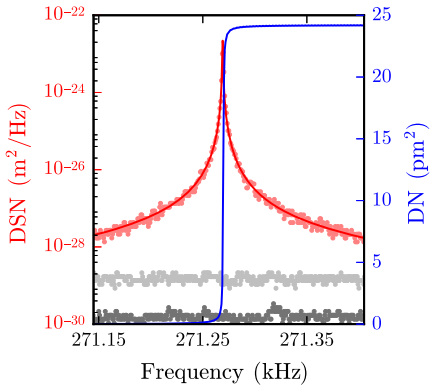

FIG. 7. Displacement spectral noise (DSN) for the fundamental mode (1,1). The calibration parameter is $V_{\rm pp} = 2.7$ V, and the best-fit values are $\omega_m^{(1,1)} = 2\pi\times 271.269$ kHz, $\Gamma^{(1,1)} = 2\pi\times 0.9$ kHz, and $m_{\rm opt}^{(1,1)} = 70.0(2)$ ng. The size of the step in the displacement noise (DN) (the blue curve), that is, the marginal of the DSN, determines the variance of the mechanical displacement $\langle x^2\rangle^{(1,1)}$ to be 24.18 pm^2.

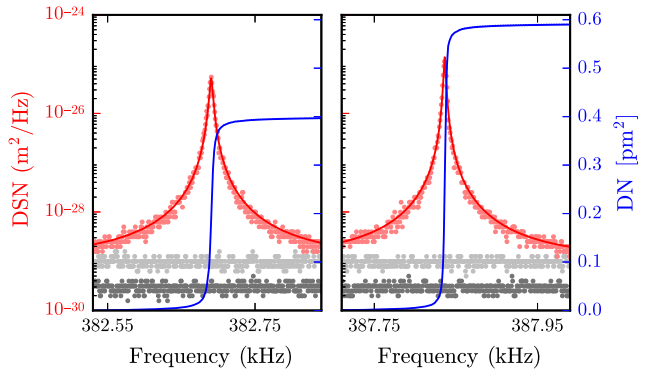

FIG. 8. Displacement spectral noise (DSN) for the doublet (1,2) and (2,1). The calibration parameter is $V_{\mathrm{pp}} = 2.8$ V. The best-fit values are $\omega_m^{(1,2)} = 2\pi \times 382.690$ kHz, $\Gamma^{(1,2)} = 2\pi \times 4.9$ Hz, $m_{\mathrm{opt}}^{(1,2)} = 1.73(1)$ μg, and $\omega_m^{(2,1)} = 2\pi \times 387.836$ kHz, $\Gamma^{(2,1)} = 2\pi \times 2.6$ Hz, and $m_{\mathrm{opt}}^{(2,1)} = 1.18(1)$ μg. The variances of the mechanical displacement are $\langle x^2\rangle^{(1,2)} \simeq 0.397$ pm^2 and $\langle x^2\rangle^{(2,1)} \simeq 0.590$ pm^2.

2. Determination of the effective mass and of the optomechanical couplings

The effective mass m_{eff} associated with a vibrational mode depends, in general, upon the mode volume and, in the case of a thin membrane, it can be written as

$$m_{\mathrm{eff}}^{(n,m)} = \int\int dxdy\sigma(x,y)u_{(n,m)}(x,y)^2, \qquad \text{(A5)}$$

where $\sigma(x,y)$ is the average mass surface density of the membrane and $u_{(n,m)}(x,y)$ is the dimensionless eigenfunction of the vibrational mode with indices (n,m) [40].

As discussed in the previous subsection, the masses obtained from the fitted thermal-noise spectra instead depend upon the optomechanical couplings $\alpha_{(n,m)}$, which differ from one mode to another because the laser beam illuminates a certain spot on the membrane, where different modes have different displacement amplitudes. After calibration of the DSN, the couplings $\alpha_{(n,m)}$ coincide with the dimensionless *transverse overlap* parameters [40], given by

$$\alpha_{(n,m)}(x,y) = \int_0^L dx' \int_0^L dy' u_{(n,m)}(x',y')I(x,y,x',y'), \qquad \text{(A6)}$$

where $I(x,y,x',y')$ is the normalized intensity profile of a laser beam centered at (x,y), and L is the length of the side of the square membrane.

In the case of our experiment, the theoretical value of Eq. (A6) can be analytically evaluated because we use a TEM_{00} Gaussian beam with waist w at the membrane position, and we verify with a finite-element-method analysis that, for the first three vibrational modes studied here, the homogeneous membrane eigenmodes, $u_{(n,m)}(x,y) = \sin(n\pi x/L)\sin(m\pi y/L)$, provide a very good approximation. Assuming negligible optical losses from clipping, the domain of integration can be extended to the entire plane, and one gets, from Eq. (A6),

$$\alpha_{nm}^{(\mathrm{th})}(x,y) = \mathrm{e}^{-w^2(k_n^2+k_m^2)/8}\sin(k_n x)\sin(k_m y), \qquad \text{(A7)}$$

where $k_n = n\pi/L$ and $k_m = m\pi/L$, both of which depend upon the unknown beam center (x,y).

One can get a very good estimate of the beam center position (x,y) (and therefore of the transverse overlaps and the physical effective masses $m_{\mathrm{eff}}^{(n,m)}$) in our setup by applying a treatment analogous to that in Ref. [26]. For each of the three detected vibrational modes, the variance of the mechanical displacement $\langle x^2\rangle^{(n,m)}$ provides an indirect estimate $(\bar{x},\bar{y})$ of (x,y) because

$$\langle x^2\rangle^{(n,m)} = \frac{k_B T}{m_{\mathrm{opt}}^{(n,m)}\omega_{nm}^2} = \alpha_{nm}^2(\bar{x},\bar{y})\frac{k_B T}{m_{\mathrm{eff}}^{(n,m)}\omega_{nm}^2}, \qquad \text{(A8)}$$

from which one derives the experimental estimate

$$\alpha_{nm}^{(\mathrm{ex})}(\bar{x},\bar{y}) \simeq \sqrt{\langle x^2\rangle^{(n,m)} m_{\mathrm{eff}}^{(n,m)}\omega_{nm}^2/k_B T}, \qquad \text{(A9)}$$

which depends upon the measured quantities $\langle x^2\rangle^{(n,m)}$, ω_{nm}^2, and T, and the unknown effective mass of the mode $m_{\mathrm{eff}}^{(n,m)}$. However, since $u_{nm}(x,y) = \sin(n\pi x/L)\sin(m\pi y/L)$ is a very good approximation, Eq. (A5) yields $m_{\mathrm{eff}}^{(n,m)} = m_T/4$ independent of (n,m), where m_T is the total mass of the membrane. Moreover, we expect that, for the fundamental mode, $\alpha_{11}^2(\bar{x},\bar{y}) \simeq 1$ because the measured waist $w = 53.2(4)$ μm is much smaller than $L = 1$ mm and the beam is centered very close to the membrane center. As a consequence, we can safely assume that $m_{\mathrm{eff}}^{(n,m)} \simeq m_{\mathrm{opt}}^{(1,1)} = 70.0(2)$ ng for the three modes in Eq. (A9), which is also consistent with the value obtained from Eq. (A5) and with the membrane specifications (1×1 mm square, a 50-nm-thick SiN membrane, and coated with a 27-nm Nb film with a 300-μm-diameter central circular hole).

We then construct the χ^2 quantity

$$\chi^2(x,y) = \sum_{n,m}[\alpha_{nm}^{(\mathrm{ex})}(\bar{x},\bar{y}) - \alpha_{nm}^{(\mathrm{th})}(x,y)]^2 \qquad \text{(A10)}$$

and minimize it over (x,y). The minimizing points (x_0,y_0) are the most likely points, and the corresponding likelihood density function of where the beam is positioned is given by [26]

$$\mathcal{L}(x,y) = \frac{1}{2\pi\sigma^2}\prod_{n,m} e^{-\{[\alpha_{nm}^{(\mathrm{ex})}(\bar{x},\bar{y}) - \alpha_{nm}^{(\mathrm{th})}(x,y)]^2/(2\sigma^2)\}}, \qquad \text{(A11)}$$

with $\sigma^2 = \chi^2(x_0,y_0)$, whose contour plot is shown in Fig. 9. The corresponding best estimation of the transverse overlap for the modes is

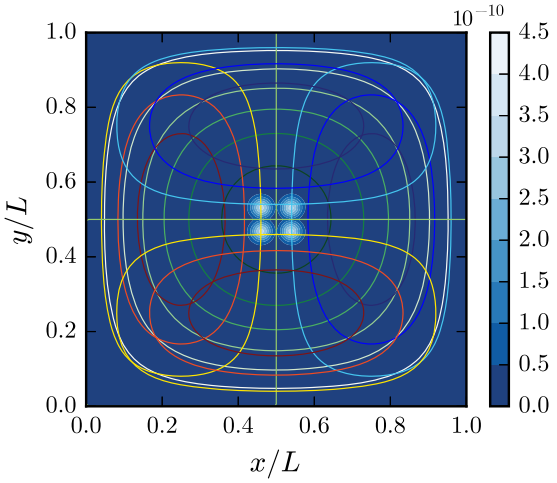

FIG. 9. Position estimates from the χ^2 minimization, showing the most likely points.

$$\alpha_{11} = 0.980, \qquad \alpha_{12} = 0.196, \qquad \alpha_{21} = 0.240, \tag{A12}$$

yielding the best estimate for the physical effective mass of the three modes, $m_{\mathrm{eff}}^{(1,1)} \simeq m_{\mathrm{eff}}^{(1,2)} \simeq m_{\mathrm{eff}}^{(2,1)} \simeq 67.3$ ng, within a 3% error, and confirmed by FEM numerical analysis.

APPENDIX B: THE ELECTROMECHANICAL COUPLINGS

As shown in Eq. (14), the electromechanical couplings G_i depend upon the explicit expression of the capacitance of the LC circuit and its dependence upon the transverse displacement associated with each vibrational normal mode of the membrane. We can write for the total capacitance $C = C_0 + C_m(\{x_i\})$, where C_0 is the capacitance of the LC circuit (including fixed and tunable capacitors), acting in parallel with the membrane capacitance $C_m(\{x_i\})$. We verify that, in our case, $C_0 \gg C_m(\{x_i\})$, so that, from Eq. (14), one can also write

$$G_i \simeq -\frac{V_{\mathrm{dc}}}{C_0}\frac{\partial C_m(\{x_i\})}{\partial x_i}\bigg|_{x_i=\bar{x}_i}. \tag{B1}$$

Following Ref. [41] and exploiting the geometry of our membrane-electrode arrangement, one can derive a theoretical model of the capacitance $C_m(\{x_i\})$ based on a quasielectrostatic calculation, which allows us to derive both the electromechanical couplings G_i and the frequency shifts of Eq. (16) and satisfactorily reproduces the data.

As shown in Fig. 2, the membrane capacitor is formed by a four-segment electrode in front of the partially metallized membrane. Since the membrane-electrode separation h_0 is significantly smaller than the interelectrode gaps, we can neglect the direct capacitance between electrode segments; the capacitance is then given by a series of two local contributions, one associated with the positive electrode segments and the membrane in front of it, C_+, and the second corresponding to the negative electrode segments, C_-, i.e.,

$$C_m = \left[\frac{1}{C_+} + \frac{1}{C_-}\right]^{-1}. \tag{B2}$$

For the calculation of $C_\pm$, we assume that the curvature of the membrane is sufficiently small that we can take it to be locally flat. We also neglect edge effects, so that for symmetry—and assuming perfect alignment—we may model the membrane-electrode capacitance locally as that of conducting parallel plates. This local capacitance per area depends only upon the local membrane-electrode separation along the direction normal to the plane defined by the electrodes, and we can write

$$C_\pm = \iint dxdy \frac{\varepsilon_0 \xi_\pm(x,y)}{h_0 + \delta z(x,y)}, \tag{B3}$$

where the integral is taken over the membrane surface, $\xi_\pm(x,y)$ is a mask function that equals 1 for points in the membrane plane that are metalized and overlap with the fixed positive or negative electrode (and zero otherwise), $\delta z(x,y)$ is the membrane displacement field relative to the steady-state configuration, and ε_0 is the vacuum dielectric constant.

We can always expand this field in terms of the vibrational eigenmodes $u_i(x,y)$ introduced in Eq. (A5)

$$\delta z(x,y) = \sum_i \beta_i u_i(x,y), \tag{B4}$$

where the eigenmodes $u_i(x,y)$ are dimensionless and the coefficients β_i are canonical drum mode position coordinates. With this notation, the derivatives appearing in the expression for the couplings of Eq. (B1) become

$$\frac{\partial C_m(\{x_i\})}{\partial x_i}\bigg|_{x_i=\bar{x}_i} \to \frac{\partial C_m}{\partial \beta_i}\bigg|_{\mathrm{eq}}, \tag{B5}$$

where the subscript eq indicates that the derivative should be evaluated at the static displacement equilibrium configuration of the membrane, $\delta z(x,y) = 0$. We have, explicitly,

$$\frac{\partial C_m}{\partial \beta_i}\bigg|_{\mathrm{eq}} = \left.\frac{\frac{1}{C_+^2}\left(\frac{\partial C_+}{\partial \beta_i}\right) + \frac{1}{C_-^2}\left(\frac{\partial C_-}{\partial \beta_i}\right)}{\left(\frac{1}{C_+} + \frac{1}{C_-}\right)^2}\right|_{\mathrm{eq}}, \tag{B6}$$

so that, using Eqs. (B3) and (B4) and inserting the results into Eq. (B1), one finally gets

$$G_i = \frac{V_{\mathrm{dc}}\epsilon_0}{C_0 h_0^2} A_i^{\mathrm{eff}}, \tag{B7}$$

where we define the effective mode area

$$A_i^{\mathrm{eff}} = \frac{\frac{O_{+,i}^{(1)}}{[O_+^{(0)}]^2} + \frac{O_{-,i}^{(1)}}{[O_-^{(0)}]^2}}{\left(\frac{1}{O_+^{(0)}} + \frac{1}{O_-^{(0)}}\right)^2}, \tag{B8}$$

in terms of the quantities

$$O_{\pm,i}^{(j)} \equiv \iint dxdy\xi_{\pm}(x,y)[u_i(x,y)]^j, \qquad j = 0, 1. \tag{B9}$$

The explicit values of the two electromechanical couplings G_1 and G_2 associated with the two mechanical modes used for our transducer can be obtained with the knowledge of C_0, V_{dc}, the distance h_0, and the various integrals $O_{\pm,i}^{(j)}$. We evaluate the latter integrals numerically from the calibrated image of the electrode and from the properly normalized finite-element numerical solution of the two vibrational eigenmodes, while C_0, and V_{dc} are easily measured. The membrane-electrode equilibrium distance h_0 is instead evaluated from the measurement of the mechanical frequency shift of the fundamental vibrational mode.

1. Derivation of the membrane-electrode distance

Equation (16) shows that each mechanical mode is shifted quadratically as a function of the applied dc voltage. A measurement of this quadratic phase shift provides a quite accurate indirect method for the determination of the distance h_0 between the metalized membrane and the electrode. In our case, we measure the frequency shift of the fundamental mode (1,1) (see Fig. 10). Denoting with $i = 0$ the fundamental mode (1,1), recalling that $C = C_0 + C_m(\{x_i\})$, with $C_0 \gg C_m(\{x_i\})$, so that $\bar{q} \simeq C_0 V_{\mathrm{dc}}$, and using Eq. (B5) and $\omega_0 = 2\pi\nu_0$, one can rewrite Eq. (16) as

$$\Delta\nu_0 = -\frac{V_{\mathrm{dc}}^2}{16\pi^2 m_{\mathrm{eff}}\nu_0}\left(\frac{\partial}{\partial\beta_0}\frac{\partial C_m}{\partial\beta_0}\right)\bigg|_{\mathrm{eq}}, \tag{B10}$$

where Eq. (B6) has to be used for the evaluation of $\partial C_m/\partial\beta_0$. It is possible to verify that

$$\left(\frac{\partial}{\partial\beta_0}\frac{\partial C_m}{\partial\beta_0}\right)\bigg|_{\mathrm{eq}} \simeq \frac{2\varepsilon_0 A_0^{\mathrm{eff}}}{h_0^3}, \tag{B11}$$

where A_0^{eff} is the effective area for the fundamental mode, and one can write

$$\nu(V_{\mathrm{dc}}) = \nu_0\left(1 - \frac{\varepsilon_0 A_0^{\mathrm{eff}}}{8\pi^2 m_{\mathrm{eff}}\nu_0^2 h_0^3}V_{\mathrm{dc}}^2\right). \tag{B12}$$

On the other hand, we can fit the experimental data of Fig. 10 with

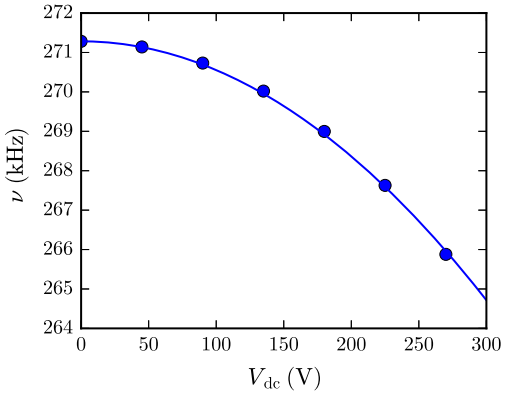

FIG. 10. Mechanical resonance frequency shift of the fundamental mode as a function of the applied dc voltage V_{dc}.

$$\nu(V_{\mathrm{dc}}) = \nu_0\left(1 - \frac{\Lambda}{8\pi^2 m_{\mathrm{eff}}\nu_0^2}V_{\mathrm{dc}}^2\right), \tag{B13}$$

where Λ is a fitting parameter. Using the best-fit values derived above, $\nu_0 = 2.712\,69$ kHz and $m_{\mathrm{eff}} = 67.3$ ng, the best-fit value of the parameter $\Lambda = 105.2(9)\ \mu\mathrm{F\,m^{-2}}$, and using $A_0^{\mathrm{eff}} = 0.3546\,\mathrm{mm^2}$ and $\epsilon_0 = 8.854\times10^{-12}\,\mathrm{F\,m^{-1}}$, the distance between the membrane and the electrode is evaluated to be

$$h_0 = \left(\frac{\varepsilon_0 A_0^{\mathrm{eff}}}{\Lambda}\right)^{1/3} \simeq 31.0(1)\ \mu\mathrm{m}. \tag{B14}$$

With this derivation of the membrane-electrode distance h_0, we can finally estimate the electromechanical couplings G_1 and G_2 using Eq. (B7) once the effective areas A_i^{eff} are estimated using Eqs. (B8) and (B9). For the mode-electrode configuration of Fig. 11, our numerical estimation gives the values of $-0.0178\ \mathrm{mm^2}$ for Fig. 11(a), $0.0189\ \mathrm{mm^2}$ for Fig. 11(b), $0.0185\ \mathrm{mm^2}$ for Fig. 11(c), and $0.0190\ \mathrm{mm^2}$ for Fig. 11(d). These values of the effective area can be understood from the fact that the blue and yellow lobes denote, respectively, the negative and positive parts of the vibrational mode function. In each of the four configurations, one of the two electrodes has approximately the same overlap with the positive and negative lobes, therefore yielding a negligible contribution to the effective area of Eq. (B8). The other electrode yields the main contribution to the effective area, which is therefore negative for Fig. 11(a) and positive for the other three cases, so that the upper configurations correspond to the constructive interference case and the lower ones to the destructive interference case.

Using these values for the effective areas and inserting $C_0 = 404$ pF, $V_{\mathrm{dc}} = 270$ V, and $h_0 = 31.0\ \mu$m into Eq. (B7), we get $G_1 = 116.4\,\mathrm{V\,m^{-1}}$ and $G_2 = -109.6\,\mathrm{V\,m^{-1}}$ for the upper electrode configurations corresponding to the constructive interference case [see Figs. 11(a) and 11(b)]. Conversely, we get $G_1 = 117.0\,\mathrm{V\,m^{-1}}$ and $G_2 = 113.9\,\mathrm{V\,m^{-1}}$

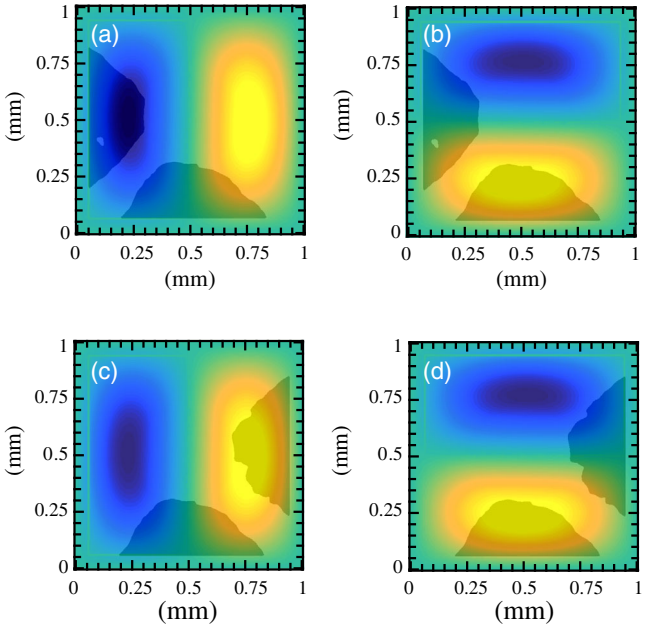

FIG. 11. Image (the gray shape) of the electrodes used (a),(b) for realizing constructive interference and (c),(d) for destructive interference overlapped with the mode shapes of the doublet obtained from a finite-element simulation. From these images, we calculate the effective areas defined in Eq. (B8) and obtain $G_1 = 116.4\ \mathrm{V\,m^{-1}}$ and $G_2 = -109.6\ \mathrm{V\,m^{-1}}$ for the upper electrode configurations, and $G_1 = 117.0\ \mathrm{V\,m^{-1}}$ and $G_2 = 113.9\ \mathrm{V\,m^{-1}}$ for the lower electrode configurations. These values are in very good agreement with the values given in the text and are obtained as best-fit parameters of the measured output spectra.

for the lower electrode configurations corresponding to the destructive interference case [see Figs. 11(c) and 11(d)]. These values are in very good agreement with the values given in the main text and are obtained as best-fit parameters of the measured output spectra.

[1] M. Aspelmeyer, T. J. Kippenberg, and F. Marquardt, Cavity optomechanics, Rev. Mod. Phys. **86**, 1391 (2014).

[2] A. D. O'Connell, M. Hofheinz, M. Ansmann, Radoslaw C. Bialczak, M. Lenander, Erik Lucero, M. Neeley, D. Sank, H. Wang, M. Weides, J. Wenner, John M. Martinis, and A. N. Cleland, Quantum ground state and single-phonon control of a mechanical resonator, Nature (London) **464**, 697 (2010).

[3] J. D. Teufel, T. Donner, Dale Li, J. W. Harlow, M. S. Allman, K. Cicak, A. J. Sirois, J. D. Whittaker, K. W. Lehnert, and R. W. Simmonds, Sideband cooling of micromechanical motion to the quantum ground state, Nature (London) **475**, 359 (2011).

[4] J. Chan, T. P. Mayer Alegre, A. H. Safavi-Naeini, J. T. Hill, A. Krause, S. Gröblacher, M. Aspelmeyer, and O. Painter, Laser cooling of a nanomechanical oscillator into its quantum ground state, Nature (London) **478**, 89 (2011).

[5] E. Verhagen, S. Deleglise, S. Weis, A. Schliesser, and T. J. Kippenberg, Quantum-coherent coupling of a mechanical oscillator to an optical cavity mode, Nature (London) **482**, 63 (2012).

[6] Amir H. Safavi-Naeini, Simon Groblacher, Jeff T. Hill, Jasper Chan, Markus Aspelmeyer, and Oskar Painter, Squeezing of light via reflection from a silicon micromechanical resonator, Nature (London) **500**, 185 (2013).

[7] T. A. Palomaki, J. D. Teufel, R. W. Simmonds, and K. W. Lehnert, Entangling mechanical motion with microwave fields, Science **342**, 710 (2013).

[8] R. W. Peterson, T. P. Purdy, N. S. Kampel, R. W. Andrews, P.-L. Yu, K. W. Lehnert, and C. A. Regal, Laser Cooling of a Micromechanical Membrane to the Quantum Backaction Limit, Phys. Rev. Lett. **116**, 063601 (2016).

[9] J. B. Clark, F. Lecocq, R. W. Simmonds, J. Aumentado, and J. D. Teufel, Observation of strong radiation pressure forces from squeezed light on a mechanical oscillator, Nat. Phys. **12**, 683 (2016).

[10] R. Riedinger, S. Hong, R. A. Norte, J. A. Slater, J. Shang, A. G. Krause, V. Anant, M. Aspelmeyer, and S. Gröblacher, Non-classical correlations between single photons and phonons from a mechanical oscillator, Nature (London) **530**, 313 (2016).

[11] Igor Pikovski, Michael R. Vanner, Markus Aspelmeyer, M. S. Kim, and Caslav Brukner, Probing planck-scale physics with quantum optics, Nat. Phys. **8**, 393 (2012).

[12] M. Bawaj, C. Biancofiore, M. Bonaldi, F. Bonfigli, A. Borrielli, G. Di Giuseppe, L. Marconi, F. Marino, R. Natali, Antonio Pontin, G. A. Prodi, E. Serra, D. Vitali, and F. Marin, Probing deformed commutators with macroscopic harmonic oscillators, Nat. Commun. **6**, 7503 (2015).

[13] J. Chaste, A. Eichler, J. Moser, G. Ceballos, R. Rurali, and A. Bachtold, A nanomechanical mass sensor with yoctogram resolution, Nat. Nanotechnol. **7**, 301 (2012).

[14] C. B. Møller, R. A. Thomas, G. Vasilakis, E. Zeuthen, Y. Tsaturyan, K. Jensen, A. Schliesser, K. Hammerer, and E. S. Polzik, Quantum back action evading measurement of motion in a negative mass reference frame, Nature (London) **547**, 191 (2017).

[15] K. Stannigel, P. Rabl, A. S. Sørensen, P. Zoller, and M. D. Lukin, Optomechanical Transducers for Long-Distance Quantum Communication, Phys. Rev. Lett. **105**, 220501 (2010).

[16] C. A. Regal and K. W. Lehnert, From cavity electromechanics to cavity optomechanics, J. Phys. Conf. Ser. **264**, 012025 (2011).

[17] J. M. Taylor, A. S. Sørensen, C. M. Marcus, and E. S. Polzik, Laser Cooling and Optical Detection of Excitations in a *LC* Electrical Circuit, Phys. Rev. Lett. **107**, 273601 (2011).

[18] Ying-Dan Wang and Aashish A. Clerk, Using Interference for High Fidelity Quantum State Transfer in Optomechanics, Phys. Rev. Lett. **108**, 153603 (2012).

[19] L. Tian, Adiabatic State Conversion and Pulse Transmission in Optomechanical Systems, Phys. Rev. Lett. **108**, 153604 (2012).

[20] Sh. Barzanjeh, M. Abdi, G. J. Milburn, P. Tombesi, and D. Vitali, Reversible Optical-to-Microwave Quantum Interface, Phys. Rev. Lett. **109**, 130503 (2012).

[21] T. Bagci, A. Simonsen, S. Schmid, L. G. Villanueva, E. Zeuthen, J. Appel, J. M. Taylor, A. Sørensen, K. Usami, A. Schliesser, and E. S. Polzik, Optical detection of radio waves through a nanomechanical transducer, Nature (London) **507**, 81 (2014).

[22] R. W. Andrews, R. W. Peterson, T. P. Purdy, K. Cicak, R. W. Simmonds, C. A. Regal, and K. W. Lehnert, Bidirectional and efficient conversion between microwave and optical light, Nat. Phys. **10**, 321 (2014).

[23] J. M. Fink, M. Kalaee, A. Pitanti, R. Norte, L. Heinzle, M. Davanco, K. Srinivasan, and O. Painter, Quantum electromechanics on silicon nitride nanomembranes, Nat. Commun. **7**, 12396 (2016).

[24] Kazuyuki Takeda, Kentaro Nagasaka, Atsushi Noguchi, Rekishu Yamazaki, Yasunobu Nakamura, Eiji Iwase, Jacob M. Taylor, and Koji Usami, Electro-mechano-optical detection of nuclear magnetic resonance, Optica **5**, 152 (2018).

[25] E. Zeuthen, A. Schliesser, A. S. Sørensen, and J. M. Taylor, Figures of merit for a quantum transducer, arXiv:1610.01099.

[26] W. H. P. Nielsen, Y. Tsaturyan, C. B. Møller, E. S. Polzik, and A. Schliesser, Multimode optomechanical system in the quantum regime, Proc. Natl. Acad. Sci. U.S.A. **114**, 62 (2017).

[27] Francesco Massel, Sung Un Cho, Juha-Matti Pirkkalainen, Pertti J. Hakonen, Tero T. Heikkilä, and Mika A. Sillanpää, Multimode circuit optomechanics near the quantum limit, Nat. Commun. **3**, 987 (2012).

[28] Atsushi Noguchi, Rekishu Yamazaki, Manabu Ataka, Hiroyuki Fujita, Yutaka Tabuchi, Toyofumi Ishikawa, Koji Usami, and Yasunobu Nakamura, Ground state cooling of a quantum electromechanical system with a silicon nitride membrane in a 3D loop-gap cavity, New J. Phys. **18**, 103036 (2016).

[29] Xu Han, Chang-Ling Zou, and Hong X. Tang, Multimode Strong Coupling in Superconducting Cavity Piezoelectromechanics, Phys. Rev. Lett. **117**, 123603 (2016).

[30] T. Caniard, P. Verlot, T. Briant, P.-F. Cohadon, and A. Heidmann, Observation of Back-Action Noise Cancellation in Interferometric and Weak Force Measurements, Phys. Rev. Lett. **99**, 110801 (2007).

[31] M. Cerdonio, L. Conti, J. A. Lobo, A. Ortolan, L. Taffarello, and J. P. Zendri, Wideband Dual Sphere Detector of Gravitational Waves, Phys. Rev. Lett. **87**, 031101 (2001).

[32] X. W. Xu, Y. Li, A. X. Chen, and Y. X. Liu, Nonreciprocal conversion between microwave and optical photons in electro-optomechanical systems, Phys. Rev. A **93**, 023827 (2016).

[33] N. R. Bernier, L. D. Tóth, A. Koottandavida, A. Nunnenkamp, A. K. Feofanov, and T. J. Kippenberg, Nonreciprocal reconfigurable microwave optomechanical circuit, Nat. Commun. **8**, 604 (2017).

[34] V. Peano, C. Brendel, M. Schmidt, and F. Marquardt, Topological Phases of Sound and Light, Phys. Rev. X **5**, 031011 (2015).

[35] G. A. Peterson, F. Lecocq, K. Cicak, R. W. Simmonds, J. Aumentado, and J. D. Teufel, Demonstration of Efficient Nonreciprocity in a Microwave Optomechanical Circuit, Phys. Rev. X **7**, 031001 (2017).

[36] Control of interference phenomena in multimode optomechanical systems for the realization of nonreciprocal devices through the control of the driving phases was exploited also in Refs. [37–39], which are, however, based on different configurations than the one demonstrated here.

[37] K. Fang, J. Luo, M. H. Matheny, F. Marquard, A. A. Clerk, and O. Painter, Generalized nonreciprocity in an optomechanical circuit via synthetic magnetism and reservoir engineering, Nat. Phys. **13**, 465 (2017);

[38] Y. Li, Y. Y. Huang, X. Z. Zhang, and L. Tian, Optical directional amplification in a three-mode optomechanical system, Opt. Express **25**, 18907 (2017);

[39] M. C. Kuzyk and H. Wang, Controlling multimode optomechanical interactions via interference, Phys. Rev. A **96**, 023860 (2017).

[40] C. Biancofiore, M. Karuza, M. Galassi, R. Natali, P. Tombesi, G. Di Giuseppe, and D. Vitali, Quantum dynamics of an optical cavity coupled to a thin semitransparent membrane: Effect of membrane absorption, Phys. Rev. A **84**, 033814 (2011).

[41] E. Zeuthen, Ph.D. thesis, University of Copenhagen, 2014.